CrossMark

A Gap-sharing Planet Pair Shaping the Crescent in HD 163296: A Disk Sculpted by a Resonant Chain

Juan Garrido-Deutelmoser[1,2] , Cristobal Petrovich[1,3] , Carolina Charalambous[4] , Viviana V. Guzmán[1,2] , and Ke Zhang[5]
[1] Instituto de Astrofísica, Pontificia Universidad Católica de Chile, Av. Vicuña Mackenna 4860, 782-0436 Macul, Santiago, Chile
[2] Núcleo Milenio de Formación Planetaria (NPF), Chile
[3] Millennium Institute for Astrophysics, Chile
[4] naXys, Department of Mathematics, University of Namur, Rue de Bruxelles 61, B-5000 Namur, Belgium
[5] Department of Astronomy, University of Wisconsin-Madison, 475 N. Charter Street, Madison, WI 53706, USA

Abstract

The Atacama Large Millimeter Array observations of the disk around HD 163296 have resolved a crescent-shape substructure at around 55 au, inside and off-center from a gap in the dust that extends from 38 to 62 au. In this work we propose that both the crescent and the dust rings are caused by a compact pair (period ratio $\simeq$4:3) of sub-Saturn-mass planets inside the gap, with the crescent corresponding to dust trapped at the L_5 Lagrange point of the outer planet. This interpretation also reproduces well the gap in the gas recently measured from the CO observations, which is shallower than what is expected in a model where the gap is carved by a single planet. Building on previous works arguing for outer planets at $\approx$86 and $\approx$137 au, we provide a global model of the disk that best reproduces the data and shows that all four planets may fall into a long resonant chain, with the outer three planets in a 1:2:4 Laplace resonance. We show that this configuration is not only an expected outcome from disk–planet interaction in this system, but it can also help constrain the radial and angular position of the planet candidates using three-body resonances.

Unified Astronomy Thesaurus concepts: Protoplanetary disks (1300); Planet formation (1241); Radiative transfer simulations (1967); Hydrodynamical simulations (767); Planetary dynamics (2173); Dust continuum emission (412); Planetary system evolution (2292); Planetary-disk interactions (2204)

1. Introduction

Substructures are ubiquitous in protoplanetary disks, particularly in the dust density distribution exhibited by high angular resolution observations (Andrews 2020; Bae et al. 2022). The Atacama Large Millimeter Array (ALMA) has revealed a variety of substructures, whereas a large population of rings and gaps are shown in continuum observations, to a lesser extent, in molecular line emissions (e.g., van der Marel et al. 2019).

The advances in spatial resolution have been able to resolve nonaxisymmetric substructures within gaps, including systems such as PDS 70 (Benisty et al. 2021), HD 163296 (Isella et al. 2018), HD 100546 (Pérez et al. 2020), HD 97048 (Pinte et al. 2019), and LkCa 15 (Long et al. 2022). These substructures may be due to embedded planets induced by gravitational interactions (e.g., Bae et al. 2022), which vary depending on the emission shape. Point-like emissions are generally associated with an accreting planet surrounded by a circumplanetary disk (Perez et al. 2015; Szulágyi et al. 2018), while crescent shapes may be related to the stable Lagrange points L_4 and L_5 of a star–planet system (Rodenkirch et al. 2021; Long et al. 2022) or vortices. These hypotheses frequently assume that a single substructure is caused by a single planet, often in a Jovian mass regime. However, we have recently shown in Garrido-Deutelmoser et al. (2022), that a pair of lower-mass and gap-sharing planets can sculpt compact, elongated, or both vortices within the gap that last for several thousand orbits.

The disk surrounding HD 163296 contains ringed structures in the millimeter-continuum (Isella et al. 2018) and several molecular tracers (Law et al. 2021; Zhang et al. 2021). In particular, inside the dust density gap that extends from 38 to 62 au, a crescent-shaped substructure resides at around 55 au (Teague et al. 2021). Recently, it was suggested that the emission comes from the dust trapped around the stable point L_5 of a Jupiter-mass planet orbiting at 48 au (Rodenkirch et al. 2021). Even though this method seems to reproduce the broad features of the dust continuum distribution, two aspects remain unclear:

1. The crescent feature resides at 55 au, off-center from the dust gap, while the L_5 point is coorbital to the planet at 48 au. Varying the planet's eccentricity to account for this shift is unlikely to help as the stability of the crescent is damaged, leading to its prompt disruption.
2. The Jupiter-mass planet, needed to retain observable amounts of dust at L_5 and open a wide enough gap in the dust, is expected to open a deep gap[6] (Duffell 2020). This prediction disagrees with the recent results provided by Zhang et al. (2021), who found that the dust density gap has a corresponding CO gap $\sim$10 times shallower than the predictions involving a Jupiter. The local gas depletion depends on the planetary mass ($\propto m_p^{-2}$; Kanagawa et al. 2015), whereby opting for a lower-mass planet to carve a shallower gap may not produce a sufficient gravitational interaction to enforce the dust trapping at L_5.

---

[6] An increase in the local viscosity to produce a much shallower gap comes at the expense of reducing the lifetime of the L_5 crescent, or even prevents its formation in the first place (Rodenkirch et al. 2021).

In this work, we propose that a compact pair of sub-Saturn-mass planets can solve these issues, simultaneously accounting for the dust emission (the shifted crescent and dust rings) and the shallow gap in the CO. This scenario is largely motivated by our recent work in Garrido-Deutelmoser et al. (2022) where we showed that a compact pair of gap-sharing planets generally lead to nonaxisymmetric substructures like that observed in HD 163296.

2. Setup

The hydrodynamics simulations and radiative transfer calculations in this work largely follow the scheme in Rodenkirch et al. (2021) and are only briefly summarized here. We carried out 2D hydrodynamic simulations using the FARGO3D multifluid code (Benítez-Llambay et al. 2019; Weber et al. 2019; Masset 2000) to produce gas and dust density distribution for a fiducial disk model. The resulting density maps are read into the RADMC3D code (Dullemond et al. 2012) to calculate the radiative transfer image at $\lambda \sim 1.25$ mm. We use this image and the HD 163296 template (that contains all the technical properties of the observation) in the SIMIO [7] package to achieve the synthetic ALMA observation comparable to the dust continuum observation provided by Isella et al. (2018).

2.1. Hydrodynamic Simulations

The initial surface density profiles for the gas (subindex g) and dust (subindex d) are given by

$$\Sigma_{\mathrm{g/d}} = \Sigma_{\mathrm{g/d},0} \left(\frac{r}{r_0} \right)^{-0.8} \exp\left[-\left(\frac{r}{r_{\mathrm{c,g/d}}} \right)^{\gamma_{\mathrm{g/d}}} \right], \qquad (1)$$

where we set $r_0 = 48$ au, the initial surface density $\Sigma_{\mathrm{g},0} = 37.4$ gr cm^{-2}, the cutoff radius $r_{\mathrm{c,g}} = 165$ au, and the exponent $\gamma_{\mathrm{g}} = 1$. Similarly, for the dust we set $\Sigma_{\mathrm{d},0} = \Sigma_{\mathrm{g},0}/100 = 0.374$ gr cm^{-2}, $r_{\mathrm{c,d}} = 90$ au, and $\gamma_{\mathrm{d}} = 2$. We include the evolution for five independent dust species. These grains have sizes in centimeters of 0.02, 0.071, 0.13, 0.26, and 1.92. We use an aspect ratio of $h(r) = h_0(r/r_0)^f$ with $h_0 = 0.05$ and a flaring index $f = 0.25$, which implies a midplane temperature profile described by $T = 25(r/r_0)^{-0.5}$ K. This setup coincides with that from Rodenkirch et al. (2021).

The disk extends from $r_{\mathrm{in}} = 5$ au to $r_{\mathrm{out}} = 197$ au, implying an initial disk mass of $\sim 0.15\,M_\odot$. The computational domain is composed of $n_{\mathrm{r}} = 512$ logarithmically spaced radial cells and $n_\theta = 768$ equally spaced cells in the azimuthal $[0, 2\pi]$ domain. We include a radially variable viscosity of the standard parameter α (Shakura & Sunyaev 1973) as

$$\alpha(r) = \alpha_{\mathrm{in}} - \frac{\alpha_{\mathrm{in}} - \alpha_{\mathrm{out}}}{2} \left[1 + \tanh\left(\frac{r - \xi}{\sigma r_0} \right) \right], \qquad (2)$$

where the inner and outer viscosities are $\alpha_{\mathrm{in}} = 1 \times 10^{-4}$ and $\alpha_{\mathrm{out}} = 5 \times 10^{-3}$, $\xi = 144$ au indicate the midpoint of the transition, and $\sigma = 1.25$ defines the slope—similar to the values provided by Liu et al. (2018).

A system of four planets was embedded. The location of the two outer ones is indicated in Teague et al. (2018) through

kinematic detections. The third planet's position (i.e., the inner planet of the outer pair) is strongly associated with the potential velocity kink reported by Pinte et al. (2020). The two inner planets are tightly packed and their parameters (masses and orbits) were derived numerically guided by the results in Garrido-Deutelmoser et al. (2022), where it was found that the planets should be gap-sharing with forming vortices at their Lagrange points, implying a condition in the planetary separation[8] of

$$\Delta a \lesssim 4.6H \simeq 11.5 \text{ au}, \qquad (3)$$

where H the scale high of the disk. In turn, the masses are constrained by the width of the gap. After a few dozen simulations attempting to match disk morphology in continuum observations at the ~ 48 au region, we choose to place the planets at $a_1 = 46$, $a_2 = 54$, $a_3 = 84.5$, and $a_4 = 137$ au with their respective masses of $M_1 = 85M_\oplus$, $M_2 = 60M_\oplus$, $M_3 = 0.4M_{\mathrm{Jup}}$, and $M_4 = 1M_{\mathrm{Jup}}$. The four bodies can gravitationally interact between them, but they do not feel the disk. We ran an extra model to compare against previous works, substituting a Jupiter at 48 au instead of the inner package of planets. Both cases were evolved for 0.48 Myr, equivalent to 2000 orbits of the innermost planet.

2.2. Radiative Transfer

We convert the 2D dust surface density into a 3D volume density assuming the vertical approximation given by

$$\rho_{\mathrm{d}_j}(r, \phi, \theta) = \frac{\Sigma(r, \phi)}{\sqrt{2\pi}\,H_{\mathrm{d}_j}} \exp\left(-\frac{z^2}{2H_{\mathrm{d}_j}^2} \right), \qquad (4)$$

where $z = r\cos(\theta)$ and the dust settling follows the diffusion model $H_{\mathrm{d}_j} = \sqrt{D_z/(D_z + \mathrm{St}_j)}\,H$, with $D_z = 0.6\alpha$ the vertical diffusion coefficient, and St_j the Stokes number of the species j (Weber et al. 2022). We assume an intrinsic volume density for the particles $\rho_s = 2$ gr cm^{-3} and a power law for the grain size distribution, such that $n(a) \propto a^{-3.5}$. We assumed a dust composition of 20% amorphous carbon, 20% water ices, and 60% silicates, where the corresponding dust opacities were computed with the code provided by Bohren & Huffman (1983). The polar direction is distributed in 64 equally spaced cells and extended in [80°.6, 99°.4] inclination domain. We use $n_{\mathrm{phot}} = 10^8$ photon packages to calculate the dust temperature, and $n_{\mathrm{scatt}} = 10^7$ photon packages to trace the thermal emission. We use a full anisotropic scattering with polarization treatment. The system is assumed to be at a distance of 101 pc with a central star of mass 1.9 $M_\odot$ and effective temperature $T_{\mathrm{eff}} = 9330$ K. The inclination is taken to be $i = 46°$ and position angle PA $= 133°$.

2.3. Synthetic Observations

We use SIMIO that contains a suite of functions for CASA 5.6.2. We select the template designed for HD 163296 to create images with the same uv-coverage as the observation from

---

[8] This expression has been tested for planets with masses near the thermal mass of $M_{\mathrm{th}} = M_\star\,h^3 \sim 0.25M_{\mathrm{J}} \simeq 80M_\oplus$.
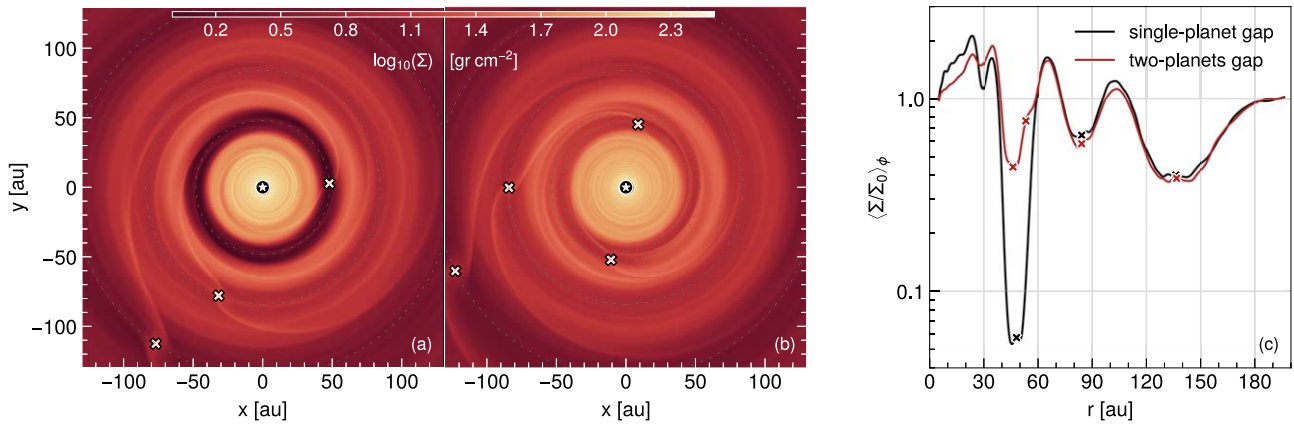
Figure 1. Panels show a time evolution after 2000 orbits at 48 au ($\sim 4.8 \times 10^5$ yr). (a) Surface density Σ maps in log-scale for a single Jupiter planet at 48 au. (b) The same as (a), but for a two-planet system with $85 M_\oplus$ and $60 M_\oplus$ instead the Jupiter. The crosses denote the position of the planets and the white lines indicate their orbits. The disk rotates in a clockwise direction. (c) Azimuthally averaged Σ/Σ_0 profiles for both models.

Isella et al. (2018). We set the rescale flux option in 0.4 to get similar intensities. In addition, we add simple thermal noise[9] of level 12 mJy to finally get rms noise of 0.022 mJy beam^{-1}.

3. Local Gap Depletion

Figure 1 shows the surface density after $\sim$0.5 Myr (2000 orbits) for the single-Jovian case (panel (a)) and the two sub-Saturns with masses $85 M_\oplus$ and $60 M_\oplus$ (panel (b)). The corresponding azimuthally averaged profiles in panel (c) show that $\sim$95% of gas is depleted for the single-Jovian, while only $\sim$55% is depleted for the two-planet case. Despite of their lower masses the planets pair creates the same gap width as the Jovian. These shallower gaps for fixed gap width are expected in compact multiplanet systems due to the planets' lower masses (depth $\Sigma_{\mathrm{gap}}/\Sigma_0 \propto M_p^{-2}$) and angular flux transferred by the neighboring planets (Duffell & Dong 2015; Garrido-Deutelmoser et al. 2022).

As argued by Zhang et al. (2021), if a Jupiter-mass planet had opened the corresponding CO gap, it would be 10 times deeper than what is actually observed. Instead, by embedding two planets we can alleviate these differences and largely reduce this discrepancy as shown in panel (c). Therefore, the depletion values would be closer to the results from observations. In order to better quantify this, we compare the CO column density gaps with the surface density from both models.[10] As shown in Figure 2, this approach reproduces the gas gap reasonably well in the two-planet case, largely matching the depths and widths with a small offset of the peaks by $\sim$4 au. In turn, the single-Jovian case is too deep compared to the observations as expected.

Beyond the third planet at $\sim$85 au, neither of the two models (single Jovian or compact pair) is able to reproduce the gas gaps. This was already noted in Zhang et al. (2021) when comparing with the models from Teague et al. (2021) and it may partly be explained by the presence of a CO snowline at 65 au. Outside the midplane CO snowline, CO freezes out at the disk midplane and therefore the CO gap properties (e.g., width and depth) may deviate from that of gas gaps due to vertical temperature and CO abundance variations. We recall
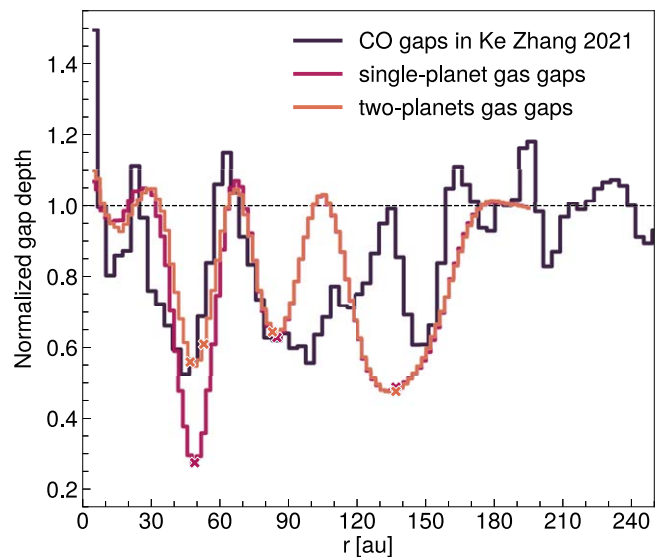

Figure 2. Comparison of column density gap in $C^{18}O$ (2–1) line observation found by Zhang et al. (2021) with gas gaps derived from surface density profiles in this work.

that our work mostly focuses on the gap and crescent at $\sim$50 au where these issues can be more securely avoided.

4. The Crescent Feature

A closely packed planet pair can directly affect the gas around each other's coorbital regions by depositing angular momentum from wave steepening and subsequent shocks. These shocks may strengthen the vorticity around the stable L_4 and L_5 Lagrange points, thus enabling the effective gas and dust trapping for at least thousands of orbital periods (Garrido-Deutelmoser et al. 2022).

The overdensity around either L_4 or L_5 for the inner and outer planet is a highly dynamic problem, with the most prominent structure chaotically alternating location. This said, we observe that for several combinations of parameters (surface density, aspect ratio, planetary masses, and so on), the outer planet often retains large amounts of material around L_5. The depicted behavior would leave an off-center substructure inside the gap that greatly reproduces the distinctive emission in the disk as shown in Figure 3. More quantitatively, our model matches the observed azimuthal extent of $\sim$45° and the radial

---

[9] https://simio-continuum.readthedocs.io/en/main/tutorials/tutorial_3.html
[10] The Σ profiles were processed under smooth function methodology described in Appendix A.
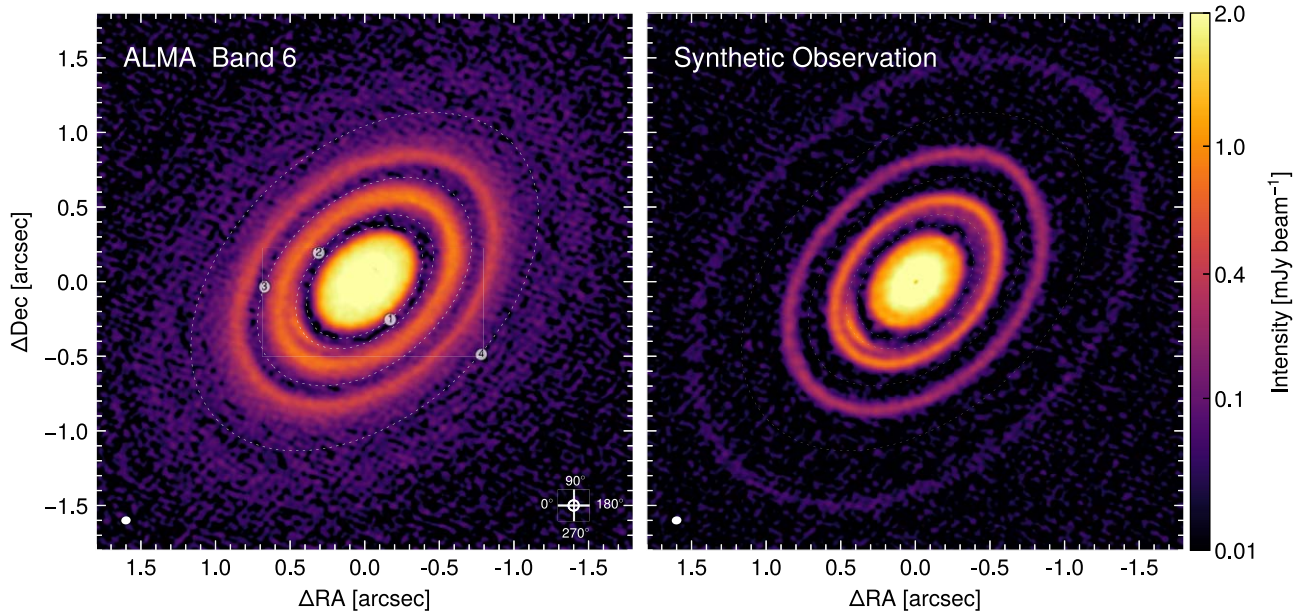
Figure 3. Band 6 ($\lambda \sim 1.25$ mm) comparison between dust continuum image from ALMA observation (Isella et al. 2018) and our synthetic observation after $\approx 4.8 \times 10^5$ yr. The synthesized beam are the same for both images ($0''.038 \times 0''.048$, $82°.5$), represented by white ellipse at the bottom left corner for each image. The synthetic image is projected with an inclination $i = 46°$ and a position angle PA = $133°$. The enumerated white dots indicate the position of potential planets associated with the following: (1) and (4) resonance angles in Laplace chains (see Section 5.1), (2) Lagrange point L_5 from the simulation, (3) velocity kink reported by Pinte et al. (2020). The white dashed lines denote the orbits of planets in the simulation. The right bottom Cartesian coordinate describes the prescription to estimate the azimuthal angles. The disk rotates in a clockwise direction.

intensity profiles passing through the crescent (peaks and troughs inside the ring at $\sim$68 au; see Appendix B for more details).

4.1. Dynamical Behavior

Figure 4 compares the gas and dust density distribution for different dust grain sizes. All the dust species show a clear shared gap between the two inner planets. In the largest size, the coorbital regions of each one display an overdensity at L_5, but the more prominent substructure belongs to the second planet. This output has taken into account two conditions. The choice of planetary masses in the inner system must be lower for the body orbiting the substructure, and the presence of the two outer planets. If we neglect either, the Lagrange points can still trap dust, but the mass distribution may change to make some L_4 or the inner L_5 the most prominent. As shown in Garrido-Deutelmoser et al. (2022), this evolution is highly dynamic and irregular so that the overdensities around L_4 and L_5 constantly change. However, the final morphology in our configuration comes from the early stages of evolution.

Theoretically, the stable Lagrange point L_5 is located at $60°$ from the planet at its trailing position. However, our model shows that the center of the crescent is slightly shifted and can vary between $65°$ and $85°$ for reasons we still do not understand and which deserve further investigation. Accordingly, the position of the proposed planet will be also slightly shifted from the Lagrange point. Finally, we observe that the azimuthal extent of the crescent remains roughly constant and equal to $\sim 45°$, similar to the observations.

4.2. Behavior for Different Dust Species

In our fiducial model, the vortensity for L_5 of the outer planet is stronger than that of the inner one (not shown). Therefore, the dust accumulation is generally expected to be greater
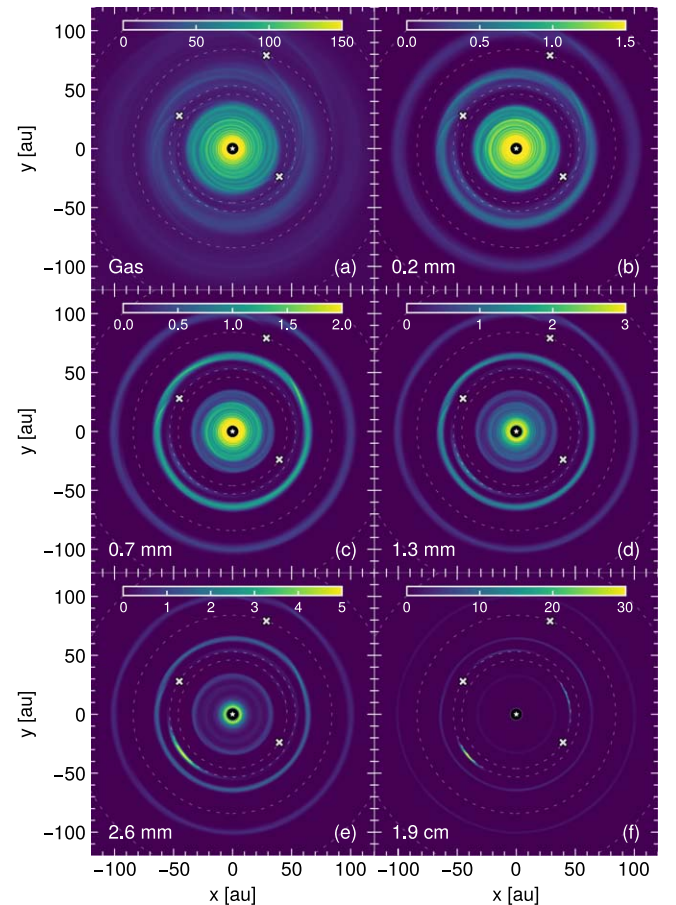

Figure 4. Face-on gas and dust surface density Σ from the hydrodynamic model after $\approx 4.8 \times 10^5$ yr (2000 orbits at 48 au). The panels correspond to different fluids. The crosses denote the position of the planets and the white dashed lines indicate their orbits. The disk rotates in a clockwise direction.

around the orbit of the outer planet for all sizes. This is especially true for small sizes that are well coupled to the gas and librate with larger amplitudes around L_5 (panels (b) and (c) in Figure 4). As the size of the grains increases (Stokes numbers approach unity, panels (d) to (f)), the dust distribution becomes compact toward the center of the Lagrange point (Montesinos et al. 2020) and we can even see some tenuous accumulation around the inner planet's L_5 point at 1.9 cm (panel (f)).

5. A Laplace Resonance Chain

Our fiducial simulation has four planets with period ratios $P_2/P_1 = (54/46)^{3/2} = 1.27$, $(84.5/54)^{3/2} = 1.96$, and $(137/84.5)^{3/2} = 2.06$. Therefore, the three outer planets lie near a 1:2:4 commensurability, which becomes nearly exact (within 1%) if planet 3 changes from 84.5 to 86 au. This fact begs the question of whether disk-driven migration may have placed the planets in their current, near-resonant orbits.[11]

From Figure 1, the planets carved relatively shallow gaps, so we may estimate the rate of orbital migration following Kanagawa & Szuszkiewicz (2020) as

$$
\tau_a \equiv \left| \frac{a}{\dot{a}} \right| \simeq \left(\frac{M_\star}{M_p} \right) \left(\frac{M_\star}{\Sigma_{min} a_p^2} \right) \frac{h_p^2}{\Omega_{K,p}},
$$

$$
\simeq 0.4\,\mathrm{Myr} \left(\frac{10\,\mathrm{gr\,cm^{-2}}}{\Sigma_{min}} \right) \left(\frac{100\,\mathrm{au}}{a_p} \right)^{1/2}
$$

$$
\times \left(\frac{2M_\odot}{M_\star} \right) \left(\frac{1M_J}{M_p} \right) \left(\frac{h_p}{0.1} \right)^2 \tag{5}
$$

where Σ_{min} corresponds to the local density at the base of the density gap. Using the fiducial planetary parameters and $M_\star = 1.9\,M_\odot$, a fixed aspect ratio $h = 0.1$, and the surface density constraints from Zhang et al. (2021, Table 5 therein), we observe that the migration timescales are all comparable to the age of the system making migration a plausible scenario.

As a proof of concept, in Figure 5 we show an N-body integration using REBOUND (Rein & Liu 2012) and prescribing the damping timescales τ_a and $\tau_e \equiv e/|\dot{e}|$ for each planet in order to mimic planet–disk interactions in the REBOUNDx library (Tamayo et al. 2019). We set $\tau_a/\tau_e = 100$ with τ_a computed using Equation (5); see the values for the orbital decay timescales in Table 1. We begin the simulations with the planets further away from their current positions and let them migrate due to their interaction with the gaseous component of the disk, where kinematic evidence has been detected in the gas at ~ 260 au (Pinte et al. 2020; Teague et al. 2021), and extensions in CO (2–1) up to ~ 500 au (Zhang et al. 2021). The evolution shows that all planet pairs are captured into a long resonant chain after $\sim 0.5 \times 10^6$ yr. These correspond to a two-body 4:3 mean-motion resonance (MMR) for the innermost planets, and a double 2:1–2:1 MMR for the two outer pairs, finally leading to the libration of the following three-body
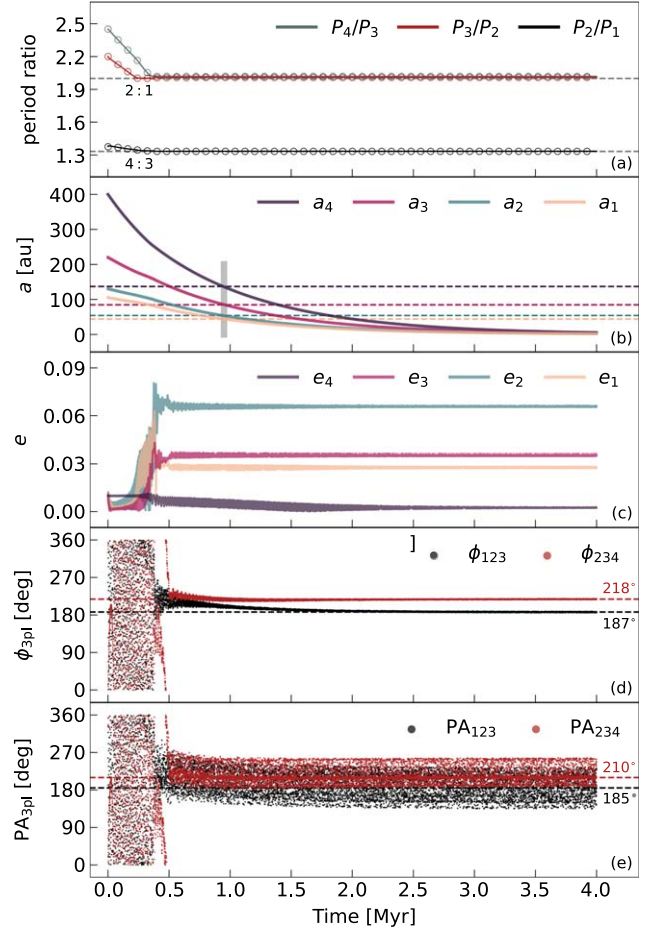
---

[11] We note that a disk-driven migration may also lead to offsets from the exact commensurabilities by either wake–planet interactions (Baruteau & Papaloizou 2013), disk-driven precession (e.g., Tamayo et al. 2015), or resonant repulsion (e.g., Papaloizou 2011).

Figure 5. Potential migratory history of the four-planet system locking the planets in a long orbital resonance chain leaving the outer three planets near a consecutive 2:1 commensurability and the innermost pair near 4:3 (panels (a) and (b)). The eccentricities remain small after the capture (panel (c)) and the three-body resonant angles $\phi_{123} = 3\lambda_1 - 5\lambda_2 + 2\lambda_3$ and $\phi_{234} = 2\lambda_2 - 6\lambda_3 + 4\lambda_4$ undergo small-amplitude libration (panel (d)). The bottom panel exhibits the corresponding combinations of the position angles in the system: $PA_{123} = 3PA_1 - 5PA_2 + 2PA_3$ and $PA_{234} = 2PA_2 - 6PA_3 + 4PA_4$.

Table 1
Migration Rate Estimates

a_p (au)	M_p ($M_\oplus$)	Σ_{min}(gr cm^{-2})	τ_a(Myr)
46	85	12	1.8
54	60	19	1.5
84.5	127	9.3	1.1
137	317	4.2	0.8

Note. The values of Σ_{min} are taken from Table 5 in Zhang et al. (2021), except for the innermost one provided by our model.

angles:

$$
\phi_{123} = 3\lambda_1 - 5\lambda_2 + 2\lambda_3, \text{ and} \tag{6}
$$

$$
\phi_{234} = 2\lambda_2 - 6\lambda_3 + 4\lambda_4. \tag{7}
$$

Both ϕ_{123} and ϕ_{234} have small-amplitude libration ($\sim 2°$) and their libration centers are 187° and 218°, respectively. Note that when the four planets reach the reported semimajor axis at approximately the same time $\sim 10^6$ yr (gray vertical line in

panel (b)), they are already captured in the two- and three-planet resonances, showing that the proposed configuration with our hydrodynamical simulations presented in the previous sections is possible.

5.1. Predicting the Position Angle (PA) of the Planet Candidates Using Three-body Resonances

Because the orbits of planets i are coplanar and nearly circular ($e_i \lesssim 0.07$), the mean longitudes λ_i are close to the true longitudes $\varpi_i + f_i$ and will likely librate around the same angles. Defining an arbitrary reference frame, rotated by PA_0 we write the position angles (PAs) as $PA_i = \varpi_i + f_i + PA_0$, and define the following three-body angle, frame-independent,[12] -combinations:

$$PA_{123} = 3PA_1 - 5PA_2 + 2PA_3, \text{ and} \qquad (8)$$

$$PA_{234} = 2PA_2 - 6PA_3 + 4PA_4. \qquad (9)$$

From panel (e) in Figure 5, we observe that these angles librate around $PA_{123} \sim 185°$ and $PA_{234} \sim 210°$ similar to ϕ_{123} and ϕ_{234}, but with larger amplitudes (near $100°$ in both cases). This is expected due to the nonzero eccentricities.

Assuming that we know two angles, say PA_2 due to the crescent and PA_3 due to a velocity kink, we can use the above relations to constrain PA_1 and PA_4 as

$$PA_1 \sim \tfrac{1}{3}PA_{123} + \tfrac{5}{3}PA_2 - \tfrac{2}{3}PA_3, \text{ and} \qquad (10)$$

$$PA_4 \sim \tfrac{1}{4}PA_{234} - \tfrac{1}{2}PA_2 + \tfrac{3}{2}PA_3. \qquad (11)$$

Our model indicates that planet 2 (54 au) is $\sim 75° \pm 10°$ ahead of the crescent center,[13] which corresponds to $PA_2 \simeq 32°$. In addition, as reported by Pinte et al. (2020), the planet 3 at 86 au has $PA_3 \simeq 357°$ associated with a velocity kink. Thus, our model predicts that the planets at 46 and 137 au should have position angles of $PA_1 \sim 237°$ and $PA_4 \sim 212°$ respectively (see the left panel in Figure 3).

Quite recently,[14] Alarcón et al. (2022) localized strong kinematic deviation in C I line emission. The position of this structure lies inside the gap at 48 au, which azimuthally coincides with our predicted planet 1 at $PA_1 \sim 237°$. We note that this predicted planet differs from the one proposed by Isella et al. (2018) and incorrectly quoted by Alarcón et al. (2022) as coincident with the outflow. The reason is that the disk rotates in a clockwise direction so the proposed planet invoked to explain the crescent as a L_5 feature, similar to Rodenkirch et al. (2021), will actually show ahead of the crescent. In this way, the C I deviation cannot be explained by a corotational planet that is also responsible for the crescent, unless the dust accumulation around L_4 becomes more prominent than that of L_5, which is unlikely (Rodenkirch et al. 2021; Garrido-Deutelmoser et al. 2022).

---

[12] Since the critical angles satisfy the D'Alembert property, these combinations are independent of the reference frame.
[13] Due to the clockwise rotation of the disk, our angle convention PA is given the coordinate axes at the bottom of Figure 3.
[14] After the submission of our manuscript to the journal.

5.2. Resonances in Other Systems

We remark that resonances may be a common outcome in these young systems, including the embedded planets in PDS 70 (Bae et al. 2019), as well as young, but disk-free systems, like HR 8799, also in a long resonance chain involving four planets (Goździewski & Migaszewski 2020).

Similar to our work, a compact multiplanet system has been proposed using the axisymmetric dust gaps and rings of HL Tau (ALMA Partnership et al. 2015), where a resonant configuration may promote the system's dynamical stability (Tamayo et al. 2015). In our case, we use not only the system's migration history and dust rings and gaps, but also add the constraints from the crescent-shape structure and the CO gas emission.

6. Conclusions

We have provided a global model for HD 163296 with four planets (semimajor axes in the range of 40–140 au) that can reproduce the rings and gaps in the dust continuum and the shallow gaps in the gas constrained by the CO emission. A key ingredient in our model is the presence of two sub-Saturn-mass planets near the 4:3 resonance opening the gap at ~ 48 au, where the crescent corresponds to the L_5 Lagrange point of the outer planet at 54 au.

We show that the four-planet system may be part of a long resonance chain with the inner two in a 4:3 MMR and the outer three in a 1:2:4 Laplace resonance chain, consistent with a history of convergent migration within the disk. Our proposed three-body resonances allow us to relate the planetary radial and angular positions, and based on the crescent location at 55 au and the proposed location by Pinte et al. (2020) for the planet at $\simeq 86$ au, our model predicts two planets: (i) a sub-Saturn at 46 au and $PA \sim 237°$; (ii) a Jovian at 137 au and $PA \sim 212°$ (Figure 3).

Overall, our work shows that tightly spaced planetary systems, often found at small orbital distances in transiting surveys, may leave detectable imprints in protoplanetary disks at much larger separations.

Software: FARGO3D (Benítez-Llambay et al. 2019), NUMPY (van der Walt et al. 2011), MATPLOTLIB (Hunter 2007). REBOUND (Rein & Liu 2012), REBOUNDX (Tamayo et al. 2019), RADMC3D (Dullemond et al. 2012).

Appendix A
Gas Gap Calculation

In Zhang et al. (2021) a smooth function was subtracted from N_{CO} column density profiles to better characterize substructures in the residual values. To compare these results with our models, we follow the same procedure. First, the Σ maps from hydrodynamic simulations were convolved with a circular Gaussian beam of $0.''15$, which has the same size as MAPS CO (2–1) line observations. Then, their azimuthally averaged profiles were interpolated every 2 au. In addition, the radial region $\{r\,[\mathrm{au}]: 0 < r_0 < 35,\ 59 < r_1 < 72,\ 98 < r_2 < 110,\ r_3 > 170\}$ was selected to describe the gaps. Both were taken as input for the SMOOTHFIT[15] module. Figure 6 shows the outputs of smoothed profile represented by the gray dashed line and the convolved surface density profile in black lines. The cyan dots denote the regions in which the function acts. Figure 2 shows the residual between lines to provide a reasonable comparison with CO gaps observations.
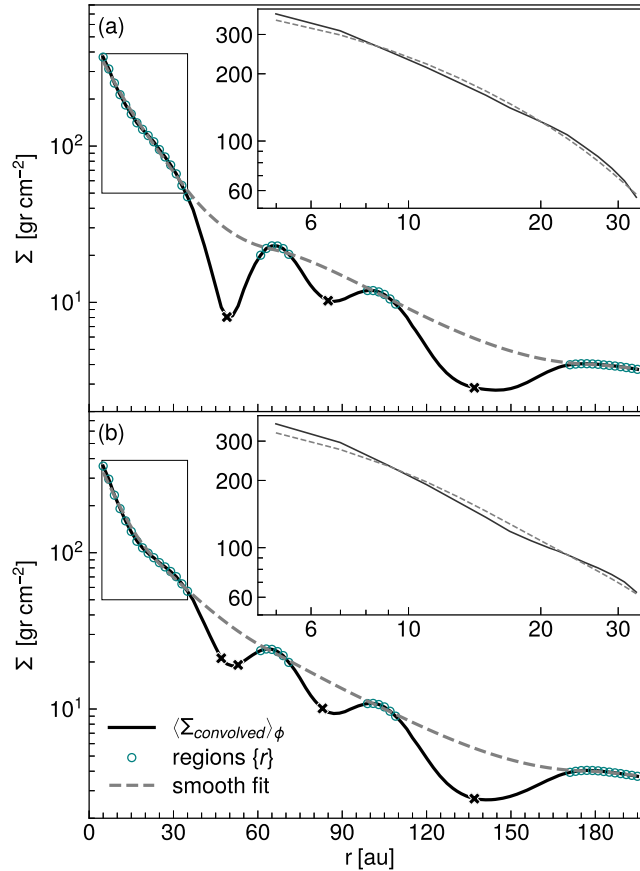

Figure 6. Black line denotes the convolved surface density profile of models and gray dashed line the respective smooth function. Panels (a) and (b) represent the single-planet case and two-planet case respectively. The crosses indicate the position of the planets.

---

[15] https://pypi.org/project/smoothfit/

Appendix B
Radial Intensity

We quantify the intensity around the substructure region of our synthetic model with the ALMA observation. First, we deproject the images obtaining a face-on view to convert them to polar coordinates and then generate a radial profile by taking the azimuthal average between PA of 300° and 350°. This extension fully covers the emission from the crescent. The results are shown in Figure 7, which is accompanied by a diagram showing the angular slice.

Figure 7 show that radial intensity through the crescent region reaches amplitudes higher than those observed by a factor of 1.2 at 55 au. The emission from the substructure is clearly off-centered on the gap and resolved in spatial resolution, showing a gap in intensity between it and the ring. The first ring reproduces the intensities in a good way, while the second is noticeably 1.7 times fainter.
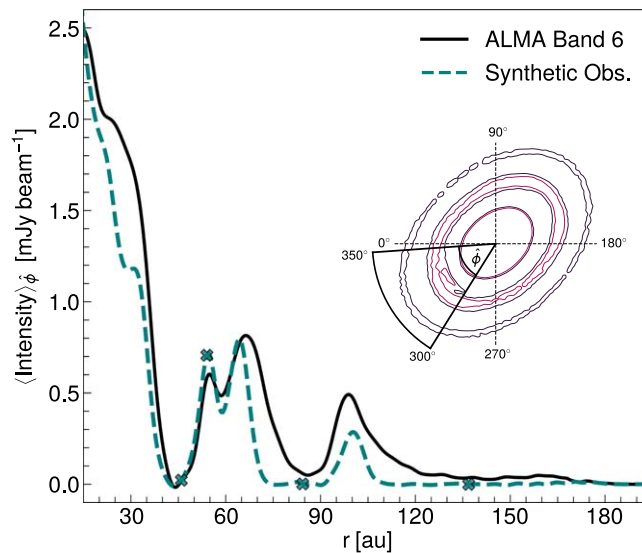

Figure 7. Azimuthally averaged intensity profiles for synthetic and ALMA observations after $\approx 4.8 \times 10^5$ yr. The crosses denote the semimajor axes of the planets. The insert shows the ALMA observation in Band 6 with contours that reproduce the crescent and rings as well as the angular slice used for the azimuthal average denoted by $\hat{\phi}$.

Appendix C
Effect from Disk Gravity Acting on Planets

We briefly test whether turning on the full disk–planet interaction may lead to morphological changes in the structure of the crescent. We recall that in our fiducial simulation (see Section 2.1), while the disk does feel the planets' gravity, the planets do not feel that of the disk.

We perform two-planet simulations considering only the inner planet pair near the 4:3 commensurability (46 and 55 au) for up to 2000 orbits of the inner planet. The initial density has been reduced by a factor of 100 to avoid significant migration. In Figure 8 we show the density distribution for two dust fluids of 0.02 and 1.9 cm grain sizes in two cases: the full disk–planet interaction is considered (left panels, displaying a slight inward migration at the ∼10% level), and the disk gravity acting on the planets is ignored (right panels, with no migration). Despite of the slight orbital migration, we do not observe any significant changes regarding the amount and distribution of captured material at the L_4 and L_5 Lagrange points.
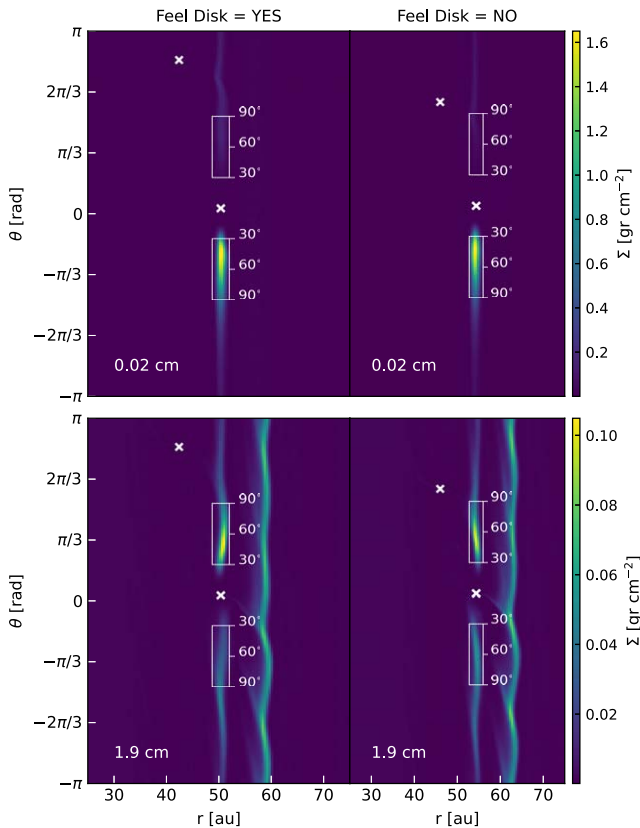

Figure 8. Dust surface density Σ for 0.02 and 1.9 cm grain sizes. The crosses denote the position of the planets. The upper and bottom white rectangles indicate the Lagrange points L_4 and L_5 with respect to the outer planet.

ORCID iDs

Juan Garrido-Deutelmoser ⓘ https://orcid.org/0000-0002-7056-3226
Cristobal Petrovich ⓘ https://orcid.org/0000-0003-0412-9314
Carolina Charalambous ⓘ https://orcid.org/0000-0002-9196-5734
Viviana V. Guzmán ⓘ https://orcid.org/0000-0003-4784-3040
Ke Zhang ⓘ https://orcid.org/0000-0002-0661-7517

References

Alarcón, F., Bergin, E. A., & Teague, R. 2022, ApJL, 941, L24
ALMA Partnership, Brogan, C. L., Pérez, L. M., et al. 2015, ApJL, 808, L3
Andrews, S. M. 2020, ARA&A, 58, 483
Bae, J., Isella, A., Zhu, Z., et al. 2022, arXiv:2210.13314
Bae, J., Zhu, Z., Baruteau, C., et al. 2019, ApJL, 884, L41
Baruteau, C., & Papaloizou, J. C. B. 2013, ApJ, 778, 7
Benisty, M., Bae, J., Facchini, S., et al. 2021, ApJL, 916, L2
Benítez-Llambay, P., Krapp, L., & Pessah, M. E. 2019, ApJS, 241, 25
Bohren, C. F., & Huffman, D. R. 1983, Absorption and Scattering of Light by Small Particles (New York: Wiley)
Duffell, P. C. 2020, ApJ, 889, 16
Duffell, P. C., & Dong, R. 2015, ApJ, 802, 42
Dullemond, C. P., Juhasz, A., Pohl, A., et al. 2012, RADMC-3D: A Multi-purpose Radiative Transfer Tool, Astrophysics Source Code Library, ascl:1202.015
Garrido-Deutelmoser, J., Petrovich, C., Krapp, L., Kratter, K. M., & Dong, R. 2022, ApJ, 932, 41
Goździewski, K., & Migaszewski, C. 2020, ApJL, 902, L40
Hunter, J. D. 2007, CSE, 9, 90
Isella, A., Huang, J., Andrews, S. M., et al. 2018, ApJL, 869, L49
Kanagawa, K. D., & Szuszkiewicz, E. 2020, ApJ, 894, 59
Kanagawa, K. D., Tanaka, H., Muto, T., Tanigawa, T., & Takeuchi, T. 2015, MNRAS, 448, 994
Law, C. J., Loomis, R. A., Teague, R., et al. 2021, ApJS, 257, 3
Liu, S.-F., Jin, S., Li, S., Isella, A., & Li, H. 2018, ApJ, 857, 87
Long, F., Andrews, S. M., Zhang, S., et al. 2022, ApJL, 937, L1
Masset, F. 2000, A&AS, 141, 165
Montesinos, M., Garrido-Deutelmoser, J., Olofsson, J., et al. 2020, A&A, 642, A224
Papaloizou, J. C. B. 2011, CeMDA, 111, 83
Pérez, S., Casassus, S., Hales, A., et al. 2020, ApJL, 889, L24
Perez, S., Dunhill, A., Casassus, S., et al. 2015, ApJL, 811, L5
Pinte, C., Price, D. J., Ménard, F., et al. 2020, ApJL, 890, L9
Pinte, C., van der Plas, G., Ménard, F., et al. 2019, NatAs, 3, 1109
Rein, H., & Liu, S.-F. 2012, A&A, 537, A128
Rodenkirch, P. J., Rometsch, T., Dullemond, C. P., Weber, P., & Kley, W. 2021, A&A, 647, A174
Shakura, N. I., & Sunyaev, R. A. 1973, A&A, 500, 33
Szulágyi, J., Plas, G. v. d., Meyer, M. R., et al. 2018, MNRAS, 473, 3573
Tamayo, D., Rein, H., Shi, P., & Hernandez, D. M. 2019, MNRAS, 491, 2885
Tamayo, D., Triaud, A. H. M. J., Menou, K., & Rein, H. 2015, ApJ, 805, 100
Teague, R., Bae, J., Aikawa, Y., et al. 2021, ApJS, 257, 18
Teague, R., Bae, J., Bergin, E. A., Birnstiel, T., & Foreman-Mackey, D. 2018, ApJL, 860, L12
van der Marel, N., Dong, R., di Francesco, J., Williams, J. P., & Tobin, J. 2019, ApJ, 872, 112
van der Walt, S., Colbert, S. C., & Varoquaux, G. 2011, CSE, 13, 22
Weber, P., Casassus, S., & Pérez, S. 2022, MNRAS, 510, 1612
Weber, P., Pérez, S., Benítez-Llambay, P., et al. 2019, ApJ, 884, 178
Zhang, K., Booth, A. S., Law, C. J., et al. 2021, ApJS, 257, 5